

Vibrational heating and photodissociation of admolecules induced by plasmonic hot carriers

Yu Chen¹ and Shiwu Gao^{1,*}

¹*Beijing Computational Science Research Center, Beijing, 100193, China*

(Dated: April 15, 2024)

Abstract

The hot carriers generated by plasmon damping hold significant potential for photoelectric conversion and photocatalysis. Despite numerous experiments and theoretical analyses, the precise role of plasmonic hot carriers in such dynamical processes has not been well understood. Here we present a theory of plasmonic photocatalysis based on the microscopic model of electron-vibrational coupling and the vibrational heating mechanism. The nonthermal hot carrier distribution was derived and treated on equal footing with the thermal Fermi-Dirac distribution. The inelastic rates of vibrational excitations were calculated including the effect of multiple electronic transitions. As an example of application, the O_2 dissociation on silver nanoparticles was explored with focus on the temperature- and light-intensity dependences. The dissociation rate evolves from a linear regime into a superlinear regime due to the onset of vibrational heating induced by hot carriers. In the nonlinear regime, nonthermal hot carriers greatly promote molecular dissociation. Our findings provide insight into plasmonic photocatalysis, and paves the way for harnessing light energies in the nonthermal regime.

I. INTRODUCTION

Optical absorption at plasmon resonance of metal nanostructures offers an efficient pathway for energy harvesting and chemical conversion, thanks to the excitation of the collective oscillations of metal conduction electrons [1–6]. These collective oscillations are scattered rapidly by various mechanisms including the metal surface, which generate hot electron-hole pairs with pronounced nonequilibrium energy distributions [7–12]. Recent experiments and simulations suggest that these plasmonic hot carriers can directly couple to semiconductors and molecules attached to the metal nanoparticles, leading to rapid carrier injections [13–18] and molecular dissociations [19–28]. Such a direct coupling results from electron tunneling and has been shown to be more efficient and faster in time scale than the internal relaxation of the metal systems [14, 17, 18, 29]. In adsorbed molecules, Raman shift of molecular vibrations has documented mode-specific vibrational temperatures, which are significantly higher than the surface temperatures on the metal nanoparticles [30, 31]. It indicates that electron-vibrational coupling under plasmon excitation is inhomogeneous among different

* swgao@csrc.ac.cn

modes within the same molecules. In the meantime, they are out of equilibrium with the metal substrate that is in contact with.

At finite temperatures, plasmon induced vibrational heating in ad molecules is inevitably competed by thermal excitations and relaxations [32, 33], both within the molecules and via the coupling to the substrate. With plasmon excitation, such a competition could be more complicated and intriguing at the hot spots of the nanoparticle aggregates [34, 35], where photothermal heating is expected to take place. How the thermal excitation interplays with the electronic coupling remains elusive and challenging for future experiment [36]. In order to disentangle the relative contributions between the electronic and thermal reaction channels [24, 27, 37, 38], it is of paramount importance to develop theoretical models for the electron-vibrational dynamics of the molecules in coupling with plasmonic hot carriers.

Recently, the Anderson-Newns model [39, 40] with a linear coupling to a harmonic oscillator has been used to describe plasmon induced vibrational excitation and photocatalysis [28] by explicitly incorporating the inelastic scattering of a bath of nonthermal hot carriers, which are generated by Landau damping of surface plasmons of metal nanoparticles [7, 8]. This model captures the basic physics of electron-vibrational coupling, nonadiabatic reaction dynamics, and the effect of hot carrier distributions. It is a versatile model in surface science for a broad range of phenomena including vibrational damping [41], electron energy loss spectroscopy [42], dissociation induced by tunneling electrons [43–45], and femtosecond laser induced desorption and dissociations [46–50]. In particular, Linic and collaborators had used this model to analyze the O_2 dissociation on silver nanoparticles (AgNP) assuming a single electron scattering event at the resonance energy [20]. With thermal and nonthermal carriers treated in the same model, it is now possible to quantify each part and compare the relative contributions from thermal and nonthermal excitations.

This paper has two objectives: First, it provides a comprehensive theoretical framework for plasmon induced hot carrier coupling and bond dissociation, which was used in our early publication at a fixed and high laser intensity [28]. This is a direct generalization of the theory of vibrational heating induced by femtosecond laser pulses [42, 47–50] with an explicit inclusion of nonthermal hot carriers. An analytical expression of vibrational transition rates for coupling with a thermal electron bath has been derived and compared with numerical evaluation. Second, based on this formulation, we explored the molecular dissociation of O_2 on AgNP, as a function of laser intensity, including the multiple electron scattering

mechanism (the so called DIMET or vibrational heating mechanism [51]). Reexcitation from vibrational excited states has been included and analyzed. We found that beyond a moderate light intensity, local vibrational heating through multiple inelastic scattering is a dominant mechanism for plasmonic photocatalysis. Our results explain the nonlinear dependence of dissociation rates at higher light intensities [20, 21] and provide insight into the mode-dependent vibrational temperatures in ad molecules [30, 31, 43]. Vibrational heating by nonthermal hot carriers is therefore a more likely mechanism than single electron scattering mechanism. It bridges the gap between the thermal versus nonthermal mechanisms for photocatalysis, which had been under debate in plasmonic photocatalysis.

The rest of the paper is organized as follows. Section II presents the formulation of our theoretical model, where different expression and approximation of the vibrational transition rates are provided and compared with numerical evaluation. The dissociation rates are then evaluated in both DIET and DIMET mechanisms. In Sec. III, the model is applied to study O_2 dissociation on AgNP with a focus on the laser-intensity dependence. As the light intensity increases, the transition from DIET to DIMET mechanism has been observed. This is accompanied with vibrational heating in the molecular bond and the appearance of nonlinear dependence of the dissociation rate. Section IV summarizes the basic conclusions and discussion.

II. MODEL

A. Hamiltonian and vibrational transition rates

The nanoparticle-molecule system is described by the Anderson-Newns model with a linear electron-vibration coupling to a truncated harmonic oscillator [41, 42, 45, 47, 52]. The total Hamiltonian is comprised of the following three parts:

$$H = H_e + H_v + H_i, \quad (1)$$

where

$$H_e = \varepsilon_a c_a^\dagger c_a + \sum_k \varepsilon_k c_k^\dagger c_k + \sum_k (v_{ak} c_a^\dagger c_k + \text{H.c.}), \quad (2a)$$

$$H_v = \hbar\Omega b^\dagger b, \quad (2b)$$

$$H_i = \lambda c_a^\dagger c_a (b^\dagger + b). \quad (2c)$$

The electronic Hamiltonian H_e consists of a molecular resonance $|a\rangle$ with energy ε_a , the continuum states of the metal nanoparticles $|k\rangle$ with energies ε_k , and the tunneling coupling v_{ak} between them. The molecular vibration H_v is approximated by a harmonic oscillator with vibrational frequency Ω .

In the resonance electron-vibration coupling, vibrational excitation is induced by the temporary occupation of the resonance state ($n_a = c_a^\dagger c_a$), resulting in vibrational motion on an excited state, which is described by a shifted harmonic oscillator with reaction coordinate q . The coupling constant λ for the linear electron-vibration interaction is determined by

$$\lambda = \sqrt{\frac{\hbar}{2\mu\Omega}} \frac{d}{dq} \varepsilon_a(q) \Big|_{q=q_0}, \quad (3)$$

where μ is the reduced mass for the oscillator, and q_0 corresponds to the equilibrium position of the ground state. Such a model Hamiltonian has been generally used to describe various surface dynamical processes in surface sciences [42, 44–49].

To describe plasmon induced photocatalysis under CW laser irradiation, it is important to consider the nonthermal hot carriers that are constantly generated by plasmonic damping. These hot carriers can couple to the molecule on a timescale given by the tunneling lifetime of the resonance state, which is typically a few femtoseconds [14, 17, 18]. It is much shorter than the thermalization time on the picoseconds for hot carriers in metals and within the nanoparticles [53–59]. Therefore, the successive and persistent generation of hot carriers by CW lasers makes it possible to maintain a nonthermal distribution on top of the thermal distribution background as given by the Fermi-Dirac distribution $f_0(\varepsilon, T)$ with an electron temperature. Neglecting the detailed dynamics of the hot carrier relaxation, the initial nonthermal distribution function can be defined by [28]

$$f_{\text{nth}}(\varepsilon) = \frac{\delta\rho(\varepsilon)}{\rho_{\text{DOS}}(\varepsilon)}. \quad (4)$$

Here $\delta\rho(\varepsilon)$ is the density response of hot carriers generated by the Landau damping of plasmons [7–11]. When normalized by the electron density of state $\rho_{\text{DOS}}(\varepsilon)$, f_{nth} can be integrated and compared with the equilibrium counterpart, f_0 of the Fermi-Dirac distribution.

For an electron bath with a general distribution function $f(\varepsilon)$, the inelastic transition rate from vibrational state $|n\rangle$ to state $|n'\rangle$ of the admolecule can be evaluated as [42, 45, 47]

$$W_{n \rightarrow n'} = \frac{4\Delta_a^2}{\pi\hbar} \int d\varepsilon f(\varepsilon)[1 - f(\varepsilon + \delta\varepsilon)] \left| \sum_m \frac{\langle n'|m\rangle \langle m|n\rangle}{\varepsilon + \varepsilon_n - \tilde{\varepsilon}_a - \varepsilon_m + i\Delta_a} \right|^2, \quad (5)$$

where $\varepsilon_n = n\hbar\Omega$ is the vibrational energy of state n , $\delta\varepsilon = \varepsilon_n - \varepsilon_{n'}$ is the energy transfer between electrons and the molecule. $\Delta_a = \sum_k \pi v_{ak}^2 \delta(\varepsilon - \varepsilon_k)$ is the broadening of molecular resonance, which effectively accounts for the tunneling coupling to the electron bath. Its Hilbert transform $\Lambda_a = \sum_k \int d\varepsilon \frac{v_{ak}^2}{\varepsilon - \varepsilon_k}$ yields the energy shift of the resonance state $\tilde{\varepsilon}_a = \varepsilon_a + \Lambda_a$.

For a hot electron bath whose energy distribution can be characterized by a Fermi-Dirac distribution with an electron temperature T_e , it is not necessarily in equilibrium with the lattice or environment. The integration over the energy distribution can be carried out, as shown in the Appendix,

$$W_{n \rightarrow n'}^{\text{th}} = \frac{4\Delta_a^2(n' - n)\Omega}{\pi} n_B(T_e, (n' - n)\hbar\Omega) \times \left| \sum_m \frac{F(m, n, n'; \beta)}{\varepsilon_F + (n' + n - 2m)\hbar\Omega/2 - \tilde{\varepsilon}_a + i\Delta_a} \right|^2, \quad (6)$$

where $n_B(T_e, \varepsilon) = [\exp(\varepsilon/k_B T_e) - 1]^{-1}$ is the Bose-Einstein distribution at T_e , $\beta = \lambda/(\hbar\Omega)$, and

$$F(m, n, n'; \beta) = \frac{\sqrt{n!n'}}{m!} e^{-\beta^2} \beta^{n+n'+2m} \times \sum_{k_1=0}^{\min[n', m]} \sum_{k_2=0}^{\min[n, m]} \frac{\binom{m}{k_1} \binom{m}{k_2}}{(-\beta^2)^{k_1+k_2} (n' - k_1)! (n - k_2)!}. \quad (7)$$

Equation (6) guarantees the detailed balance between vibrational transitions, $W_{n \rightarrow n'}^{\text{th}}/W_{n' \rightarrow n}^{\text{th}} = \exp[(\varepsilon_n - \varepsilon_{n'})/k_B T_e]$. In Appendix, this expression is compared with the exactly numerical evaluations and a more simplified expression derived earlier [47]. When the lattice and the electron bath are in equilibrium at the same temperature, equation (6) represents the vibrational transition rate without laser irradiation, namely the dark condition.

To incorporate the nonthermal hot carriers generated by the laser irradiation, the electron distribution function can be generalized to include the nonthermal term as

$$f(\varepsilon, T) = f_0(\varepsilon, T) + f_{\text{nth}}(\varepsilon), \quad (8)$$

since these nonthermal hot carriers also participate in the molecular scattering and vibrational excitation. In order to separate the thermal and nonthermal contributions, the product between distribution functions in Eq. (5) is partitioned into four parts,

$$\begin{aligned} f(\varepsilon)(1 - f(\varepsilon + \delta\varepsilon)) &= (f_0(\varepsilon) + f_{\text{nth}}(\varepsilon))[1 - (f_0(\varepsilon + \delta\varepsilon) + f_{\text{nth}}(\varepsilon + \delta\varepsilon))] \\ &= f_0(\varepsilon)(1 - f_0(\varepsilon + \delta\varepsilon)) + f_{\text{nth}}(\varepsilon)(1 - f_0(\varepsilon + \delta\varepsilon)) \\ &\quad - f_0(\varepsilon)f_{\text{nth}}(\varepsilon + \delta\varepsilon) - f_{\text{nth}}f_{\text{nth}}(\varepsilon + \delta\varepsilon). \end{aligned} \quad (9)$$

Here the first term corresponds to the contribution from the thermal distributions. Due to the tiny magnitude of f_{nth} compared to f_0 , the last term is much smaller and can therefore be neglected. The second and third terms correspond to the contributions from the nonthermal hot electrons and hot holes, respectively, namely

$$\begin{aligned} W_{n \rightarrow n'}^{\text{nth}} &= W_{n \rightarrow n'}^{\text{HE}} + W_{n \rightarrow n'}^{\text{HH}}, \\ W_{n \rightarrow n'}^{\text{HE}} &= \frac{4\Delta_a^2}{\pi\hbar} \int d\varepsilon f_{\text{nth}}(\varepsilon)(1 - f_0(\varepsilon + \delta\varepsilon)) \left| \sum_m \frac{\langle n'|m\rangle\langle m|n\rangle}{\varepsilon + \varepsilon_n - \tilde{\varepsilon}_a - \varepsilon_m + i\Delta_a} \right|^2, \\ W_{n \rightarrow n'}^{\text{HH}} &= -\frac{4\Delta_a^2}{\pi\hbar} \int d\varepsilon f_0(\varepsilon)f_{\text{nth}}(\varepsilon + \delta\varepsilon) \left| \sum_m \frac{\langle n'|m\rangle\langle m|n\rangle}{\varepsilon + \varepsilon_n - \tilde{\varepsilon}_a - \varepsilon_m + i\Delta_a} \right|^2. \end{aligned} \quad (10)$$

Equation (10) can be numerically evaluated. It provides an unambiguous and concise way to calculate the nonthermal transition rates from hot electrons and holes, which was done in an ad hoc way by dividing the distributions into three energy regimes [28].

In the truncated harmonic oscillator approximation for the ground state potential energy surface (PES), molecular dissociation occurs when the vibrational energy surpasses the dissociation barrier. By considering the vibrational transition from all bound states up to the dissociation level, n_d , the dissociation rate under laser excitation is given by:

$$R_{\text{dis}} = \sum_{n=0}^{n_d-1} p_n(T) W_{n \rightarrow n_d}, \quad (11)$$

where $p_n(T)$ is the thermal population of vibrational state n at temperature T . For reaction induced by single electronic transition (DIET regime), their vibrational populations follow exactly the Bose-Einstein statistics at electronic temperature T_e , which is assumed to be in thermal equilibrium with the environment.

B. Vibrational heating in the DIMET regime

The rate of dissociation in the DIET mechanism accounts only for a single inelastic scattering from a bound state. It does not include possible modification of vibrational populations by the multiple inelastic scattering of nonthermal carriers in the DIMET regime. Experimentally, DIMET can naturally occur under high laser irradiations or in plasmonic gaps with strong local field enhancement [20, 21, 60]. Vibrational heating can be described efficiently by introducing a modified vibrational temperature T_v , which in principle should be determined by solving the master equation [45, 47].

A simple and approximate way to determine the vibrational temperature in DIMET can be obtained by extracting the temperature from the vibrational transitions between the ground state $n = 0$ and the $n = 1$ excited state, $W_{0 \rightarrow 1}^{\text{tot}} = \Gamma_{\uparrow}^{\text{tot}}$ and $W_{1 \rightarrow 0}^{\text{tot}} = \Gamma_{\downarrow}^{\text{tot}}$,

$$T_v = \frac{\hbar\Omega}{k_B \ln \left(\frac{\Gamma_{\downarrow}^{\text{tot}}}{\Gamma_{\uparrow}^{\text{tot}}} \right)} = \frac{\hbar\Omega}{k_B \ln \left(\frac{\Gamma_{\downarrow}^{\text{th}} + \Gamma_{\downarrow}^{\text{nth}}}{\Gamma_{\uparrow}^{\text{th}} + \Gamma_{\uparrow}^{\text{nth}}} \right)}. \quad (12)$$

With the vibrational temperature, the dissociation rate within the DIMET mechanism can now be evaluated using the modified vibrational populations $p_n = n_B(T_v, \varepsilon_n)$. We will later discuss the effect of the DIMET mechanism and make comparison with the DIET mechanism.

III. RESULTS AND DISCUSSIONS

Here we apply the model of Sec. II to study the vibrational excitation and dissociation of O_2 AgNP which has been intensively investigated experimentally [19, 20]. Upon adsorption, the O-O bond lies parallelly to the surface [61–63], suggesting no direct coupling between molecular dipole and the local field. Hence, direct photodissociation by the electric field can be ruled out and the hot carrier mechanism is expected to be dominant. To describe the electronic structure of AgNP, We adopt a jellium sphere model [7, 8, 13] for the ground state spectrum of spherical nanoparticles with a diameter up to $D = 25$ nm and the Wigner-Seitz radius $r_s/r_B = 3.02$, where r_B is the Bohr radius. The adsorbate-specific parameters are extracted from first-principle calculations of O_2 chemisorbed on the Ag(100) [20], with $\Delta_a = 0.6$ eV, $\varepsilon_a = 2.4$ eV corresponding to the $2\pi^*$ resonance of the O_2 on Ag(100) surface,

and $\hbar\Omega = 0.10$ eV being the vibrational energy of the adsorbed O-O stretch mode. The barrier of dissociation will be investigated as a parameter, as its value should depend on the specific local geometry of the molecular adsorption on the AgNP surface.

A. Hot carrier distribution

As a first step, the nonthermal distribution defined in Eq. (4) is first evaluated as a function of wavelength and laser intensity. Figure 1 shows the energy and wavelength dependences of the nonthermal distribution function. When illuminated by light with given energy $h\nu$, the hot carriers generated are essentially distributed within the energy range $(\varepsilon_F, \varepsilon_F + h\nu)$ for the electrons and $(\varepsilon_F - h\nu, \varepsilon_F)$ for the holes, respectively. Both distributions of electrons and holes are plotted by the absolute magnitude. For a given particle size D and carrier lifetime τ , the nonthermal carriers are distributed predominantly near the Fermi level due to the available thermal electron-hole pairs near the Fermi surface. The hot carriers are therefore affected by the populations of thermal electron-hole pairs during Landau damping. Apart from this thermal character, there are purely nonthermal distributions at energies far away from the Fermi level. Increasing the carrier lifetime or reducing the nanoparticle size favors the hot carrier distribution and thus enhances the nonthermal distributions [7]. In the dependence of photon energy, a clear resonance enhancement can be observed at $h\nu \sim 3.5$ eV, which coincides with the calculated plasmon resonance $\hbar\omega_p$ of the AgNP at the given diameter [64]. This resonance effect confirms that the plasmon excitation is dominant in hot carrier generations.

Figure 2 shows the hot carrier distributions as a function of the light intensity. These distributions have the same energy profiles. The magnitude of the distributions depends linearly on the light intensity I_0 , as expected by the linear response theory. Under near-resonant excitation, the local field experienced by the conduction electrons is dominated by the plasmonic field, whose intensity scales linearly with that of the incident light. We have not considered any nonlinear response of the field.

Figure 3 shows in more detail the total hot carrier distribution function at $T = 500$ K including both the Fermi-Dirac distribution and the nonthermal distribution. The overall distribution is dominated by the thermal distribution, as expected. Nonthermal distributions are substantially smaller in magnitude for the low-energy electrons and holes near the Fermi

level. However, away from the Fermi level, the thermal distributions exponentially decay while the nonthermal distributions do not. It implies that the high-energy distributions should always be dominated by the nonthermal electron-hole pairs. To help understand the different contributions from the thermal and nonthermal carriers, we qualitatively divide the total distribution function into three regions. The thermal (TH) region near the Fermi level contains both thermal and nonthermal components, but is overwhelmingly dominated by the thermal carriers. The hot hole (HH) and hot electron (HE) regions predominantly consist of hot holes and hot electrons, respectively. The insets are close ups of distributions in the HH and HE regions.

B. Rates of vibrational transitions

To investigate how the nonthermal hot carriers affect the vibrational excitation of the molecules adsorbed on the nanoparticle surface, we plot in Fig. 4(a) the rate of vibrational excitation $W_{0 \rightarrow 1}$ as a function of temperature with separate contributions from hot electrons (red line), hot holes (blue line) and thermal carriers (black line). For vibrational transition with small inelastic energy transfer, direct thermal activation still dominates with rates 2-4 orders of magnitude higher than those of the hot electrons and hot holes. Thermal contribution shows temperature dependence, those of hot electrons and hot holes are temperature independent, in accordance with their nonthermal character. Moreover, due to location of the energy resonance, the vibrational coupling between high-energy hot electrons with the unoccupied O_2 $2\pi^*$ orbital is more efficient than the hot holes, leading to larger vibrational excitation rates for the hot electrons.

The lower panel of Fig. 4(b) further shows the rate of vibrational transition to a higher $n = 6$ state, where a larger amount of energy transfer is involved in the inelastic scattering. The larger energy transfer required is inefficient for thermal excitation, which reaches only 10^{-11} s^{-1} even at a high temperature of 500 K. Instead, the rates induced by hot electrons is much more efficient, while rates of hot holes are higher than the thermal excitations at low temperatures. From Fig. 4(a) and Fig. 4(b), we can conclude that the nonthermal hot electrons provide efficient channels in activating vibrational excitation and barrier crossing of the admolecule, and are dominant for transitions involving larger inelastic energy transfer in the low temperature regime. This conclusion was demonstrated at a very high CW light

intensity (10^{12} W/m²) in the previous publication [28].

Figure 5(a) shows the light intensity dependence of $W_{0\rightarrow1}$ at a fixed temperature of 300 K. Contributions from different carriers are presented in the same way as shown in Fig. 4(b). Here, the nonthermal contributions increase linearly with the light intensity as expected from the linear response theory. It is clear that the thermal excitation dominates $W_{0\rightarrow1}$ under weak illumination, and is overtaken by hot electrons for light intensities higher than $\sim 4 \times 10^9$ W/m². On the contrary, for $W_{0\rightarrow6}$ shown in Fig. 5(b), the hot electrons remain as the most efficient channel across the entire region of light intensity under study. The light intensity dependence of the inelastic transition rates suggests that the nonthermal hot electrons plays an important role in activating molecular bond even at much lower light intensities.

C. Dissociation rate in the vibrational heating mechanism

We next analyze the dissociation rate of O₂ on AgNP. A laser with $h\nu = 3.5$ eV is used for resonance plasmon excitation. Figure 6 shows the dissociation rate as a function of light intensity in the DIET mechanism. The variation of dissociation barrier is modeled by different dissociation level n_d in the truncated harmonic oscillator model. Overall, the dissociation rate is very sensitive to n_d , and low energy barrier favors dissociation as expected by the Arrhenius law. This is evidently verified in Fig. 6, where the magnitude of dissociation rate is much larger at smaller n_d . Besides, all the dissociation rates show linear dependence on the light intensity as expected in the DIET mechanism. Such a linear dependence remains to even lower intensities, because the dissociation rate involves large inelastic energy transfer and is dominantly activated by the nonthermal hot carriers.

As light intensity increases, successive inelastic scatterings may induce local vibrational heating within the molecular bond, which modifies local vibrational distributions and leads to a vibrational temperature higher than that of the environment [30, 31, 43]. Such a vibrational heating mechanism was found to dominate the surface desorption and reactions induced by femtosecond laser pulses [46–50, 60]. Recently, it was also discussed that the DIET mechanism was not sufficient to account for plasmonic photocatalysis [20, 21], where the superlinear light intensity dependence has been observed at a not-so-high (10^3 - 10^4 W/m²) laser intensity. Nonlinear intensity dependence is usually a clear signature of

local vibrational heating due to multiple electronic scatterings [47, 49–51, 60].

Figure 7(a) shows the vibrational temperature, T_v , calculated by Eq. (10) as a function of light intensity at three environmental temperatures $T_{\text{env}} = T_e = 200, 300$, and 400 K, respectively. At low light intensities, vibrational heating is negligible. The vibrational temperatures (solid lines) can hardly be distinguished from the electronic temperatures (dashed lines). As the light intensity increases, the inelastic vibrational excitation gradually populates higher vibrational states, modifying the detailed balance and lifting the vibrational temperatures T_v to a higher value than T_e . Indeed, higher vibrational temperature of ad molecule was reported using Raman thermometry [30, 31] as a signature of plasmonic photocatalysis. The onset of vibrational heating starts at lower intensities when the environmental temperature is decreased. At $I_0 = 10^{10}$ W/m², the temperature increase in T_v reaches ~ 180 K at $T_e = 200$ K, but is only ~ 95 K at $T_e = 400$ K. Figure 7(a) suggests that the vibrational heating mechanism is the dominant mechanism in plasmonic photocatalysis in the high intensity regime. Such a local heating in the vibrational mode is much more efficient for chemical energy transfer and does not necessarily involve much increase in lattice temperature.

The enhanced vibrational temperature directly affects the rate of dissociation, which involves contributions from multiple electronic transitions. As shown in Fig. 7(b), the dissociation rate follows similar trend as the vibrational temperature, but shows more sensitive dependences in magnitude. At low light intensities, the dissociation rate is predominantly determined by the DIET mechanism and thus follows a linear intensity dependence (dashed lines). These rates (solid lines) deviate from their DIET curves as the light intensity increases due to vibrational heating (see Fig. 7(a)), and evolve into a superlinear intensity dependence. In the low temperature regime, where the vibrational heating is more dramatic, a more rapid and significant increase of superlinearity can be observed. We can therefore conclude that the multiple electronic scatterings dominate the dissociation in the high intensity regime, whereas in low intensity regime, the dissociation is still dominated by the single electronic transition.

Figure 8 shows the light intensity dependence of the dissociation rate for different dissociation barriers, and the comparison with those in the DIET mechanism (dashed lines) as shown in Fig. 6. The dissociation rates are superlinear in the DIMET regime and are much higher in magnitude. At light intensity (10^{10} W/m²), the superlinear rates correspond to a

power-law dependence with a nonlinear exponent of $n = 3.0$, $n = 4.2$, $n = 5.2$, and $n = 6.2$, for $n_d = 4$, $n_d = 6$, $n_d = 8$ and $n_d = 10$, respectively. From the theory of vibrational heating [45–47, 49, 51, 60, 65], this nonlinear exponent corresponds to a robust number of inelastic scatterings that is required for the molecule to reach dissociation.

Figure 9 displays the dissociation rate as a function of temperature in the vibrational heating mechanism. The black solid line shows the dissociation rate at dark condition, and essentially follows the Arrhenius law. With light irradiation, nonthermal activation of molecular dissociation starts to operate and enhances significantly the rate of dissociation. This effect is more drastic as the temperature decreases. In all these calculations, we used resonant laser excitation and the dissociation level of $n_d = 6$. At increasing temperature, which yields population of higher vibrational states, dissociation by the excitation from the vibrationally excited states becomes more efficient, which equivalently diminishes the effect of the nonthermal carriers. From Fig. 9, we conclude that plasmonic hot carriers can promote photodissociation mostly in low temperature and high-light intensity regime, where multiple inelastic scattering by the nonthermal hot carriers becomes efficient and dominant.

While the model captures essential feature of nonthermal hot carriers in the rate of plasmonic photodissociation and its transition from linear to superlinear light intensity dependence, the calculated threshold ($\sim 10^8$ W/m²) of the transition is considerably higher than the light intensity measured in the experiment ($\sim 10^3$ W/m²) [20]. This difference between theory and experiment could largely result from the extra local field enhancement present at the plasmonic gaps in experiment. Typically, the experiment was performed on ensemble of nanocubes, where the photodissociation mostly take place at hot spots in narrow plasmonic gaps. The local field therein is substantially higher than the surface field on a single spherical nanoparticle as treated in our calculations. For instance, the field enhancement at the hot spot of the nanoparticle dimer can be more than 3 orders of magnitude higher than that near an individual nanoparticle [20, 66]. This local field argument is also consistent with the experimental observation that single nanoparticle did not yield photodissociation at the same experimental conditions [20]. In addition, dynamics beyond one-dimensional harmonic oscillator, and possible inhomogeneous density distribution of hot carriers, which are neglected in our model but may present in larger nanoparticles as used in experiment, may also contribute to the quantitative discrepancy.

IV. CONCLUSION

Based on the Anderson-Newns model of resonance electron-vibration coupling and an explicit derivation of nonthermal hot carrier distribution, we have presented a theoretical description of vibrational heating and dissociation induced by plasmonic hot carriers, with the focus on the mechanism of plasmon induced photocatalysis. As an application of the model, we analyzed the photodissociation of O_2 adsorbed on AgNP and systematically examined the dissociation rate as functions of temperature and light intensity. Introduction of the nonthermal distribution function enables us to quantify the contribution of nonthermal carriers and compare with that of thermal carriers on equal footing under CW laser illumination. The results demonstrate that a small fraction of population by energetic nonthermal carriers is sufficient to greatly enhance the vibrational excitation, thus promoting the catalytic dissociation, especially in the low temperature regime. Furthermore, single electronic scattering dominates the dissociation under weak excitation, multiple electronic scatterings start to dominate as the light intensity increases. The transition from linear to superlinear dependence of dissociation rate has been found, which is in accordance with experimental observation. Our model captures the essential physics underlying the mechanism of plasmonic catalysis, and reproduces the features of experimental measurement. It paves the way to optimize the efficiency of plasmonic light harvesting and energy transformations.

ACKNOWLEDGMENTS

This work was supported by the National Natural Science Foundation of China (11934003, 12393831, U2230402). The authors would like to thank Dr. Yang Jiao and Dr. Shenxiang Wu for helpful discussions.

APPENDIX: EVALUATION OF $W_{n \rightarrow n'}$ INDUCED BY HOT CARRIERS WITH A THERMAL DISTRIBUTION

Here we evaluate the inelastic transition rate between two vibrational states $|n\rangle$ and $|n'\rangle$ induced by thermal hot carriers. By taking the Fermi-Dirac distribution $f_0(\varepsilon, T_e)$ with an

electron temperature T_e in Eq. (5), the rate reads

$$W_{n \rightarrow n'}^{\text{th}} = \frac{4\Delta_a^2}{\pi\hbar} \int d\varepsilon f_0(\varepsilon, T_e) [1 - f_0(\varepsilon + \delta\varepsilon, T_e)] \times \left| \sum_m \frac{\langle n'|m\rangle \langle m|n\rangle}{\varepsilon + \varepsilon_n - \tilde{\varepsilon}_a - \varepsilon_m + i\Delta_a} \right|^2. \quad (\text{A1})$$

Without explicitly calculating the Franck-Condon factors $\langle n'|m\rangle$ (and $\langle m|n\rangle$) and based on the assumption $\Delta_a \gg \hbar\Omega$, an approximate expression in the limit of weak electron-vibration coupling was previously derived as [47]

$$W_{n \rightarrow n'} \simeq \frac{4\Delta_a^2(\varepsilon_{n'} - \varepsilon_n)}{\pi\hbar} \frac{n_{>}!}{n_{<}!} \times \frac{\lambda^{2(n_{>} - n_{<})}}{\{[\varepsilon_F + (\varepsilon_{n'} + \varepsilon_n)/2 - \tilde{\varepsilon}_a]^2 + \Delta_a^2\}^{n_{>} - n_{<} + 1}} \times n_B(T_e, \varepsilon_{n'} - \varepsilon_n), \quad (\text{A2})$$

where $n_{>} = \max\{n, n'\}$, $n_{<} = \min\{n, n'\}$. We go beyond some of these approximations by taking the Franck-Condon factors analytically, and arrive at an improved expression valid in more general conditions.

The molecular vibration has been approximated by a harmonic oscillator $H_p = \hbar\Omega b^\dagger b$, whose ground PES is approximated by a truncated harmonic oscillator. With the linear electron-vibration coupling mediated by the occupancy of the local resonance, the excited state is represented by a shifted harmonic oscillator $H_p^* = \hbar\Omega b^\dagger b + \lambda(b^\dagger + b)$. The Franck-Condon factor is the wavefunction overlap between two harmonic oscillators shifted by a distance $\delta_q = |\lambda\sqrt{2/(\mu\hbar\Omega^3)}|$, which can be evaluated analytically [67]. In particular, we further assumed that the PESs of the ground state $|n\rangle$ and the temporarily negative ion state $|m\rangle$ for O_2 adsorbed on AgNP have the same force constant as suggested by first-principal calculations [19, 20]. The general expression [67] is then reduced to a more compact form as

$$\langle n|m\rangle = \begin{cases} e^{-\frac{\beta^2}{2}} \beta^{n-m} \sqrt{\frac{m!}{n!}} L_m^{n-m}(\beta^2), & n \geq m, \\ (-1)^{m-n} e^{-\frac{\beta^2}{2}} \beta^{m-n} \sqrt{\frac{n!}{m!}} L_n^{m-n}(\beta^2), & n \leq m, \end{cases} \quad (\text{A3})$$

where $\beta = (\mu\Omega/2\hbar)^{1/2}\delta_q = \lambda/\hbar\Omega$, and

$$L_n^\alpha = \sum_{l=0}^n (-1)^l \binom{n+\alpha}{n-l} \frac{\beta^l}{l!} \quad (\text{A4})$$

is the generalized Laguerre polynomial.

Based on the fact that the distribution function $f_0(\varepsilon, T_e)$ is fast varying around the Fermi level, the product $f_0(\varepsilon, T_e)[1 - f_0(\varepsilon + \delta\varepsilon, T_e)]$ has a maximum at $\varepsilon_F - \delta\varepsilon/2$ and dominates in a range within $\sim k_B T_e$. The energy integration in (A1) can therefore be performed by moving the square of module, whose variation is small within $k_B T_e$, out of the integrand. Combining with Eq. (A3), the vibrational transition rate mediated by thermal hot carriers reads

$$W_{n \rightarrow n'}^{\text{th}} \simeq \frac{4\Delta_a^2(\varepsilon_{n'} - \varepsilon_n)}{\pi\hbar} \times \left| \sum_m \frac{F_{m,n,n'}}{\varepsilon_F + (\varepsilon_{n'} + \varepsilon_n)/2 - \varepsilon_a - \varepsilon_m + i\Delta_a} \right|^2 \times n_B(T_e, \varepsilon_{n'} - \varepsilon_n), \quad (\text{A5})$$

with

$$F_{m,n,n'} = \frac{\sqrt{n!n'!}}{m!} e^{-\beta^2} \beta^{n+n'+2m} \times \sum_{k_1=0}^{\min[n',m]} \sum_{k_2=0}^{\min[n,m]} \frac{\binom{m}{k_1} \binom{m}{k_2}}{(-\beta^2)^{k_1+k_2} (n' - k_1)! (n - k_2)!}. \quad (\text{A6})$$

In Tab. I we compare the results of $W_{n \rightarrow n'}^{\text{th}}$ evaluated by three different methods. For the transition with low energy transfer ($W_{0 \rightarrow 1}$), Eq. (A5) shows good agreement with both Eq. (A2) derived earlier [47] and that by numerical integration of Eq. (A1). However, Eq. (A5) is more accurate than Eq. (A2) for vibrational transition involving larger energy transfer as in ($W_{0 \rightarrow 6}$), it is comparable with the direct numerical evaluation.

	$W_{0 \rightarrow 1}^{\text{th}} \text{ (s}^{-1}\text{)}$	$W_{0 \rightarrow 6}^{\text{th}} \text{ (s}^{-1}\text{)}$
Eq. (A1)	9.08×10^7	2.05×10^{-14}
Eq. (A5)	9.04×10^7	1.25×10^{-14}
Eq. (A2) [47]	1.05×10^8	8.87×10^{-14}

TABLE I. $W_{n \rightarrow n'}^{\text{th}}$ evaluated by different methods.

[1] C. Clavero, *Nat. Photonics* **8**, 95 (2014).

[2] S. Linic, U. Aslam, C. Boerigter, and M. Morabito, *Nat. Mater.* **14**, 567 (2015).

- [3] M. L. Brongersma, N. J. Halas, and P. Nordlander, [Nat. Nanotechnol. **10**, 25 \(2015\)](#).
- [4] J. G. Smith, J. A. Fauchaux, and P. K. Jain, [Nano Today **10**, 67 \(2015\)](#).
- [5] U. Aslam, V. G. Rao, S. Chavez, and S. Linic, [Nat. Catal. **1**, 656 \(2018\)](#).
- [6] C. Zhan, M. Moskovits, and Z.-Q. Tian, [Matter **3**, 42 \(2020\)](#).
- [7] A. Manjavacas, J. G. Liu, V. Kulkarni, and P. Nordlander, [ACS Nano **8**, 7630 \(2014\)](#).
- [8] A. O. Govorov and H. Zhang, [J. Phys. Chem. C **119**, 6181 \(2015\)](#).
- [9] R. Sundararaman, P. Narang, A. S. Jermyn, W. A. Goddard III, and H. A. Atwater, [Nat. Commun. **5**, 5788 \(2014\)](#).
- [10] M. Bernardi, J. Mustafa, J. B. Neaton, and S. G. Louie, [Nat. Commun. **6**, 7044 \(2015\)](#).
- [11] A. M. Brown, R. Sundararaman, P. Narang, W. A. Goddard III, and H. A. Atwater, [ACS Nano **10**, 957 \(2015\)](#).
- [12] H. Reddy, K. Wang, Z. Kudyshev, L. Zhu, S. Yan, A. Vezzoli, S. J. Higgins, V. Gavini, A. Boltasseva, P. Reddy, V. M. Shalae, and E. Meyhofer, [Science **369**, 423 \(2020\)](#).
- [13] A. O. Govorov, H. Zhang, and Y. K. Gun'ko, [J. Phys. Chem. C **117**, 16616 \(2013\)](#).
- [14] K. Wu, J. Chen, J. R. McBride, and T. Lian, [Science **349**, 632 \(2015\)](#).
- [15] S. K. Cushing, C.-J. Chen, C. L. Dong, X.-T. Kong, A. O. Govorov, R.-S. Liu, and N. Wu, [ACS Nano **12**, 7117 \(2018\)](#).
- [16] G. Tagliabue, J. S. DuChene, M. Abdellah, A. Habib, D. J. Gosztola, Y. Hattori, W.-H. Cheng, K. Zheng, S. E. Canton, R. Sundararaman, J. Sá, and H. A. Atwater, [Nat. Mater. **19**, 1312 \(2020\)](#).
- [17] J. Ma and S. Gao, [ACS Nano **13**, 13658 \(2019\)](#).
- [18] J. Ma, X. Zhang, and S. Gao, [Nanoscale **13**, 14073 \(2021\)](#).
- [19] P. Christopher, H. Xin, and S. Linic, [Nat. Chem. **3**, 467 \(2011\)](#).
- [20] P. Christopher, H. Xin, A. Marimuthu, and S. Linic, [Nat. Mater. **11**, 1044 \(2012\)](#).
- [21] S. Mukherjee, F. Libisch, N. Large, O. Neumann, L. V. Brown, J. Cheng, J. B. Lassiter, E. A. Carter, P. Nordlander, and N. J. Halas, [Nano Lett. **13**, 240 \(2012\)](#).
- [22] S. Mukherjee, L. Zhou, A. M. Goodman, N. Large, C. Ayala-Orozco, Y. Zhang, P. Nordlander, and N. J. Halas, [J. Am. Chem. Soc. **136**, 64 \(2014\)](#).
- [23] L. Zhou, C. Zhang, M. J. McClain, A. Manjavacas, C. M. Krauter, S. Tian, F. Berg, H. O. Everitt, E. A. Carter, P. Nordlander, and N. J. Halas, [Nano Lett. **16**, 1478 \(2016\)](#).
- [24] L. Zhou, D. F. Swearer, C. Zhang, H. Robatjazi, H. Zhao, L. Henderson, L. Dong, P. Christo-

- pher, E. A. Carter, P. Nordlander, and N. J. Halas, *Science* **362**, 69 (2018).
- [25] C. Hu, X. Chen, J. Jin, Y. Han, S. Chen, H. Ju, J. Cai, Y. Qiu, C. Gao, C. Wang, Z. Qi, R. Long, L. Song, Z. Liu, and Y. Xiong, *J. Am. Chem. Soc.* **141**, 7807 (2019).
 - [26] Q. Wu, L. Zhou, G. C. Schatz, Y. Zhang, and H. Guo, *J. Am. Chem. Soc.* **142**, 13090 (2020).
 - [27] L. Zhou, M. Lou, J. L. Bao, C. Zhang, J. G. Liu, J. M. P. Martirez, S. Tian, L. Yuan, D. F. Swearer, H. Robatjazi, E. A. Carter, P. Nordlander, and N. J. Halas, *Proc. Natl. Acad. Sci.* **118**, e2022109118 (2021).
 - [28] S. Wu, Y. Chen, and S. Gao, *Phys. Rev. Lett.* **129**, 086801 (2022), due to a mistake in the numerical implementation, the laser intensity used here was underestimated by three orders of magnitude.
 - [29] M. Bonn, S. Funk, C. Hess, D. N. Denzler, C. Stampfl, M. Scheffler, M. Wolf, and G. Ertl, *Science* **285**, 1042 (1999).
 - [30] C. Boerigter, R. Campana, M. Morabito, and S. Linic, *Nat. Commun.* **7**, 10545 (2016).
 - [31] C. Boerigter, U. Aslam, and S. Linic, *ACS Nano* **10**, 6108 (2016).
 - [32] Y. Dubi and Y. Sivan, *Light Sci. Appl.* **8**, 89 (2019).
 - [33] Y. Dubi, I. W. Un, and Y. Sivan, *Chem. Sci.* **11**, 5017 (2020).
 - [34] A. O. Govorov, W. Zhang, T. Skeini, H. Richardson, J. Lee, and N. A. Kotov, *Nanoscale Res. Lett.* **1**, 84 (2006).
 - [35] G. Baffou, P. Berto, E. Bermúdez Ureña, R. Quidant, S. Monneret, J. Polleux, and H. Rigneault, *ACS Nano* **7**, 6478 (2013).
 - [36] G. Baffou, I. Bordacchini, A. Baldi, and R. Quidant, *Light Sci. Appl.* **9**, 108 (2020).
 - [37] X. Zhang, X. Li, M. E. Reish, D. Zhang, N. Q. Su, Y. Gutierrez, F. Moreno, W. Yang, H. O. Everitt, and J. Liu, *Nano Lett.* **18**, 1714 (2018).
 - [38] C. Zhan, B. W. Liu, Y. F. Huang, S. Hu, B. Ren, M. Moskovits, and Z. Q. Tian, *Nat. Commun.* **10**, 2671 (2019).
 - [39] P. W. Anderson, *Phys. Rev.* **124**, 41 (1961).
 - [40] D. M. Newns, *Phys. Rev.* **178**, 1123 (1969).
 - [41] B. N. J. Persson and M. Persson, *Solid State Commun.* **36**, 175 (1980).
 - [42] J. W. Gadzuk, *Phys. Rev. B* **44**, 13466 (1991).
 - [43] S. Gao, *Surf. Sci.* **313**, 448 (1994).
 - [44] B. C. Stipe, M. A. Rezaei, W. Ho, S. Gao, M. Persson, and B. I. Lundqvist, *Phys. Rev. Lett.*

- [78](#), 4410 (1997).
- [45] S. Gao, M. Persson, and B. I. Lundqvist, [Phys. Rev. B](#) **55**, 4825 (1997).
 - [46] D. G. Busch, S. Gao, R. A. Pelak, M. F. Booth, and W. Ho, [Phys. Rev. Lett.](#) **75**, 673 (1995).
 - [47] S. Gao, [Phys. Rev. B](#) **55**, 1876 (1997).
 - [48] S. Gao, B. I. Lundqvist, and W. Ho, [Surf. Sci.](#) **341**, L1031 (1995).
 - [49] S. Gao, D. G. Busch, and W. Ho, [Surf. Sci.](#) **344**, L1252 (1995).
 - [50] T. Olsen, J. Gavnholt, and J. Schiøtz, [Phys. Rev. B](#) **79**, 035403 (2009).
 - [51] J. A. Misewich, T. F. Heinz, and D. M. Newns, [Phys. Rev. Lett.](#) **68**, 3737 (1992).
 - [52] N. S. Wingreen, K. W. Jacobsen, and J. W. Wilkins, [Phys. Rev. B](#) **40**, 11834 (1989).
 - [53] S. Link, C. Burda, Z. L. Wang, and M. A. El-Sayed, [J. Chem. Phys.](#) **111**, 1255 (1999).
 - [54] C. Voisin, D. Christofilos, N. Del Fatti, F. Vallée, B. Prével, E. Cottancin, J. Lermé, M. Pellarin, and M. Broyer, [Phys. Rev. Lett.](#) **85**, 2200 (2000).
 - [55] J. Y. Bigot, J. Y. Merle, O. Cregut, and A. Daunois, [Phys. Rev. Lett.](#) **75**, 4702 (1995).
 - [56] A. Arbouet, C. Voisin, D. Christofilos, P. Langot, N. D. Fatti, F. Vallée, J. Lermé, G. Celep, E. Cottancin, M. Gaudry, M. Pellarin, M. Broyer, M. Maillard, M. P. Pileni, and M. Treguer, [Phys. Rev. Lett.](#) **90**, 177401 (2003).
 - [57] J. R. M. Saavedra, A. Asenjo-Garcia, and F. J. García de Abajo, [ACS Photonics](#) **3**, 1637 (2016).
 - [58] J. G. Liu, H. Zhang, S. Link, and P. Nordlander, [ACS Photonics](#) **5**, 2584 (2017).
 - [59] A. M. Brown, R. Sundararaman, P. Narang, A. M. Schwartzberg, W. A. Goddard, and H. A. Atwater, [Phys. Rev. Lett.](#) **118**, 087401 (2017).
 - [60] D. G. Busch and W. Ho, [Phys. Rev. Lett.](#) **77**, 1338 (1996).
 - [61] L. Vattuone, P. Gambardella, U. Valbusa, and M. Rocca, [Surf. Sci.](#) **377-379**, 671 (1997).
 - [62] S. Messerli, S. Schintke, K. Morgenstern, J. Nieminen, and W.-D. Schneider, [Chem. Phys. Lett.](#) **328**, 330 (2000).
 - [63] J. R. Hahn and W. Ho, [J. Chem. Phys.](#) **123**, 214702 (2005).
 - [64] P. B. Johnson and R. W. Christy, [Phys. Rev. B](#) **6**, 4370 (1972).
 - [65] F.-J. Kao, D. G. Busch, D. Gomes da Costa, and W. Ho, [Phys. Rev. Lett.](#) **70**, 4098 (1993).
 - [66] N. J. Halas, S. Lal, W.-S. Chang, S. Link, and P. Nordlander, [Chem. Rev.](#) **111**, 3913 (2011).
 - [67] F. Iachello and M. Ibrahim, [J. Phys. Chem. A](#) **102**, 9427 (1998).

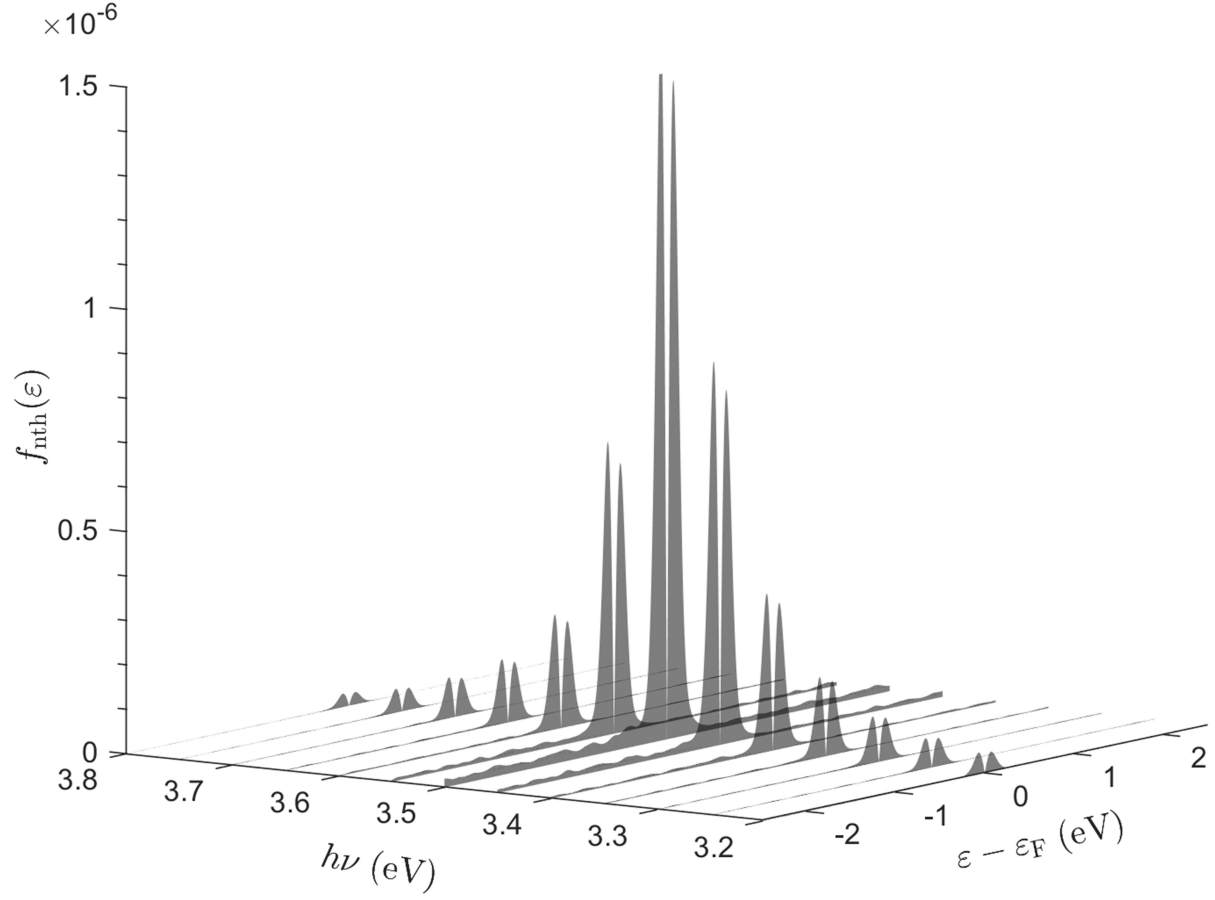


FIG. 1. Wavelength dependence of the nonthermal energy distribution of plasmonic hot carriers. A significant resonance enhancement appears at $h\nu = 3.5$ eV, corresponding to the plasmon resonance of a silver sphere with diameter $D = 25$ nm. The calculations are taken at $T = 300$ K, $I_0 = 10^7$ W/m², and $\tau = 100$ fs.

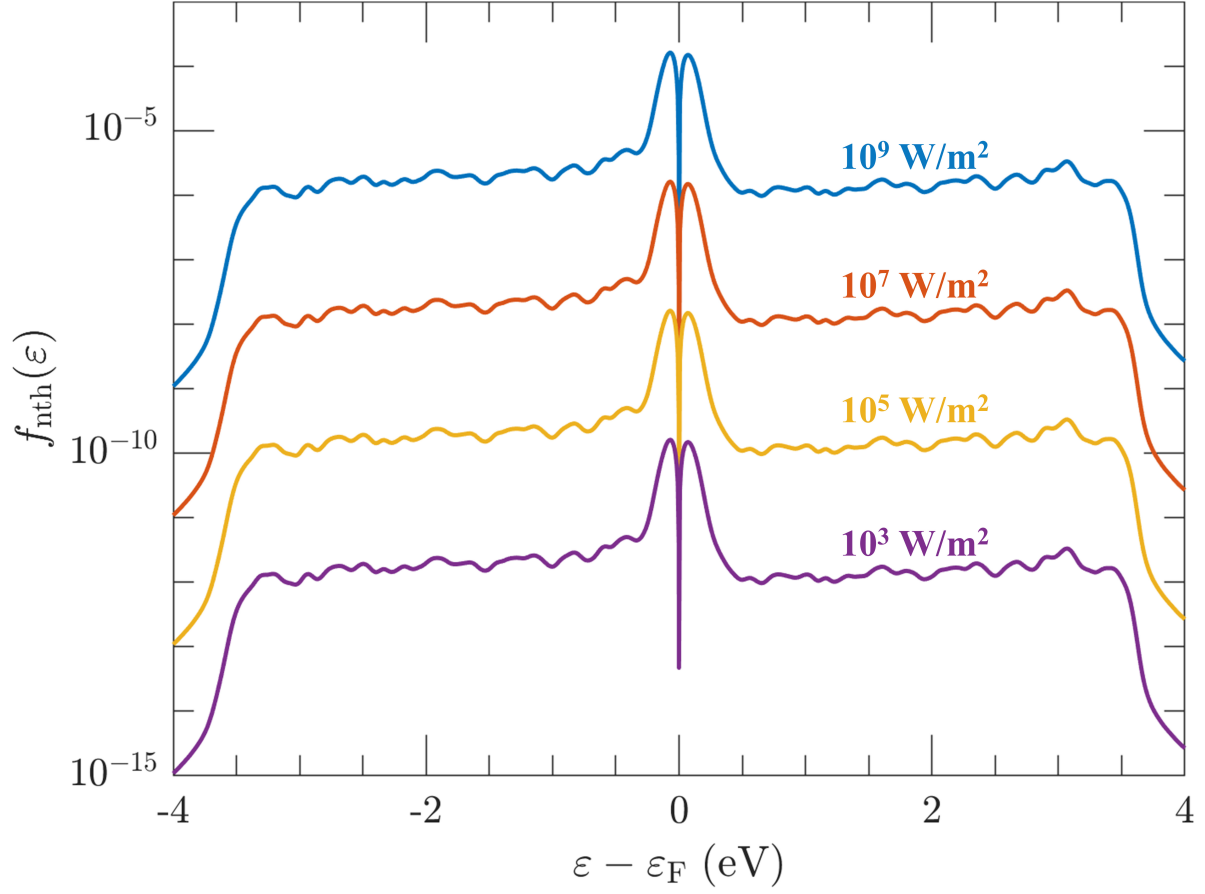


FIG. 2. The nonthermal energy distribution of plasmonic hot carriers under resonant excitation $h\nu = 3.5$ eV at different light intensities. Based on the linear response framework, the hot carrier generation depends linearly on light intensity. Other parameters used in the calculations are $T = 300$ K and $\tau = 100$ fs.

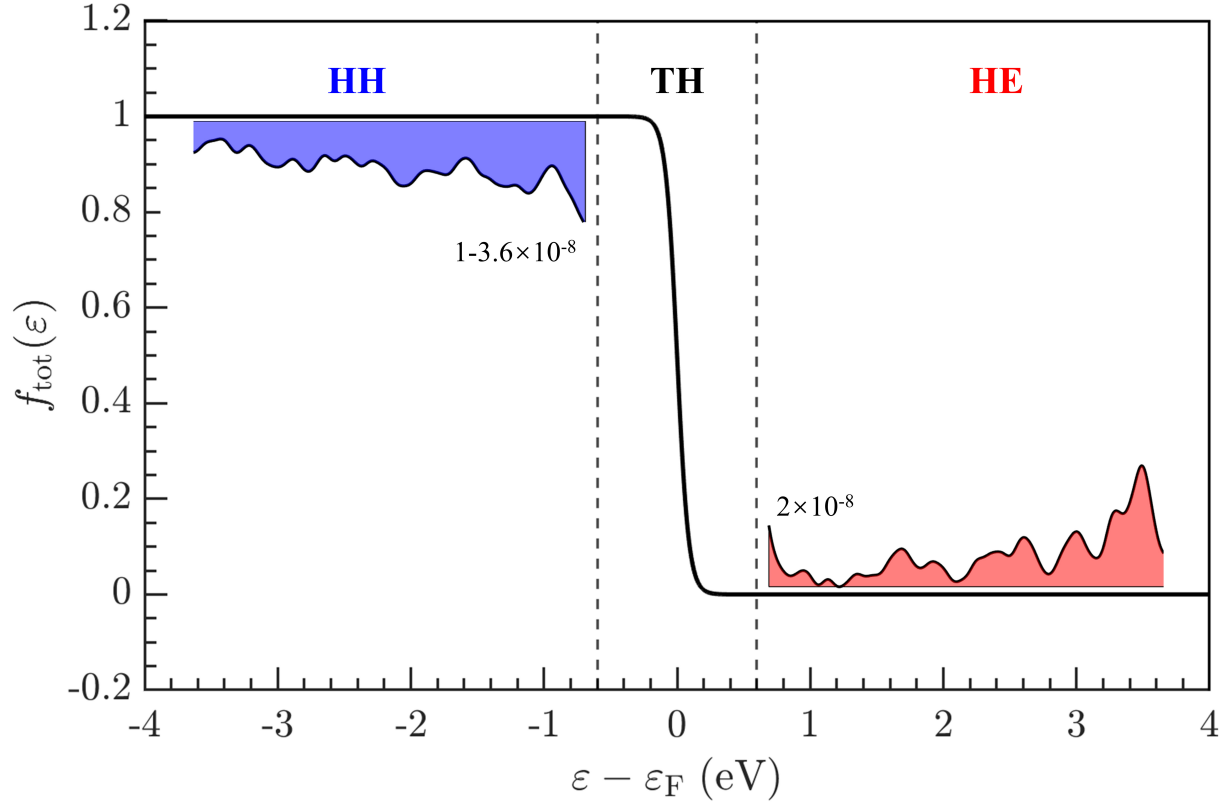


FIG. 3. The total electronic energy distribution at $T = 500$ K and $I_0 = 10^7$ W/m². Carriers are segmented into three regions. The TH region around the Fermi level contains mostly the thermal carriers, while the HH and HE regions consist of hot holes and hot electrons, respectively. The nonthermal characters are colored for clarification.

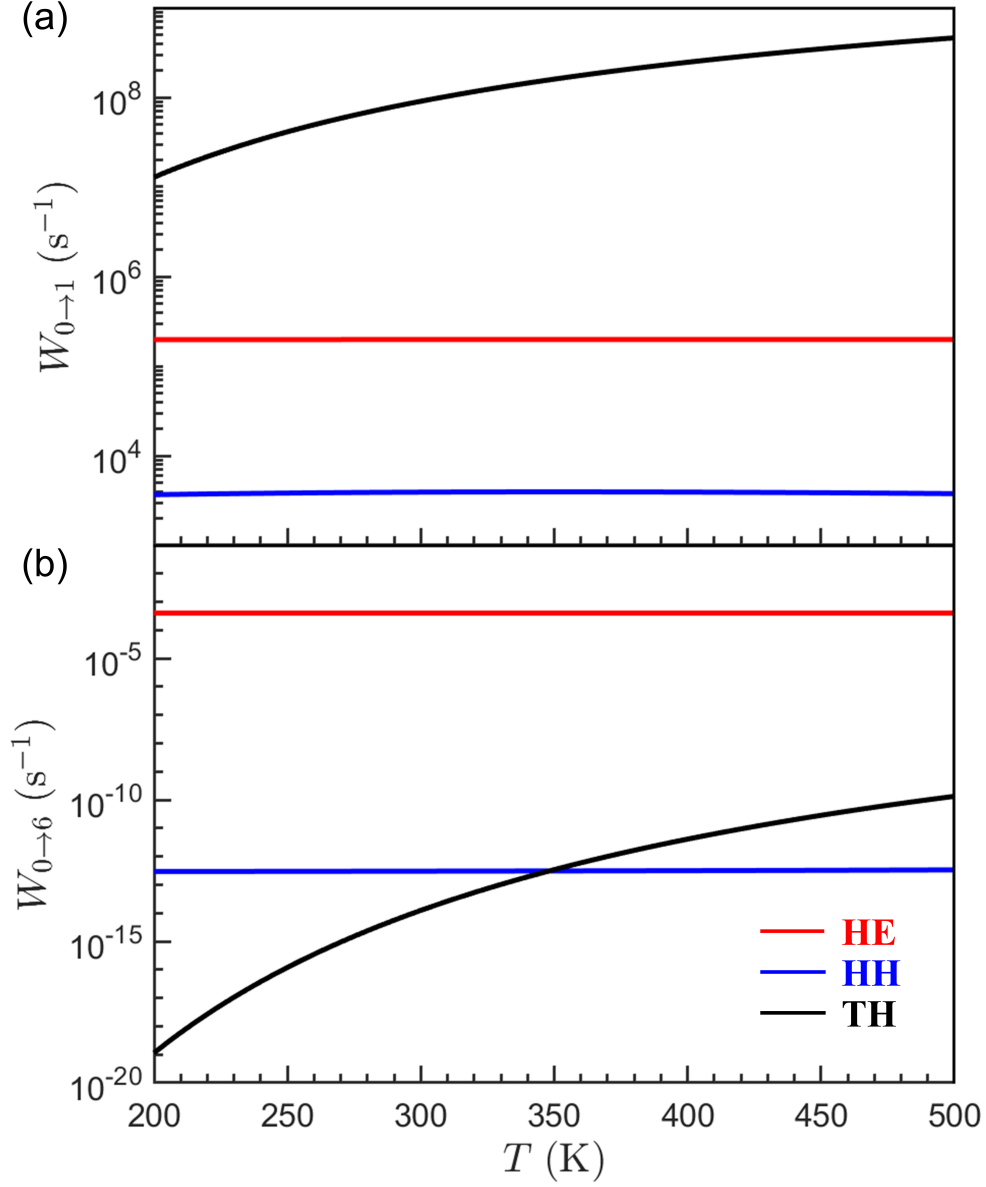


FIG. 4. Temperature dependence of the vibrational excitation rate with the light intensity fixed at 10^7 W/m^2 . Contributions from hot electrons (red lines), hot holes (blue lines), and thermal carriers (black lines) to both (a) $n = 0$ to $n = 1$ and (b) $n = 0$ to $n = 6$ excitations are evaluated. The nonthermal carriers are efficient in promoting the activation of molecular vibrations.

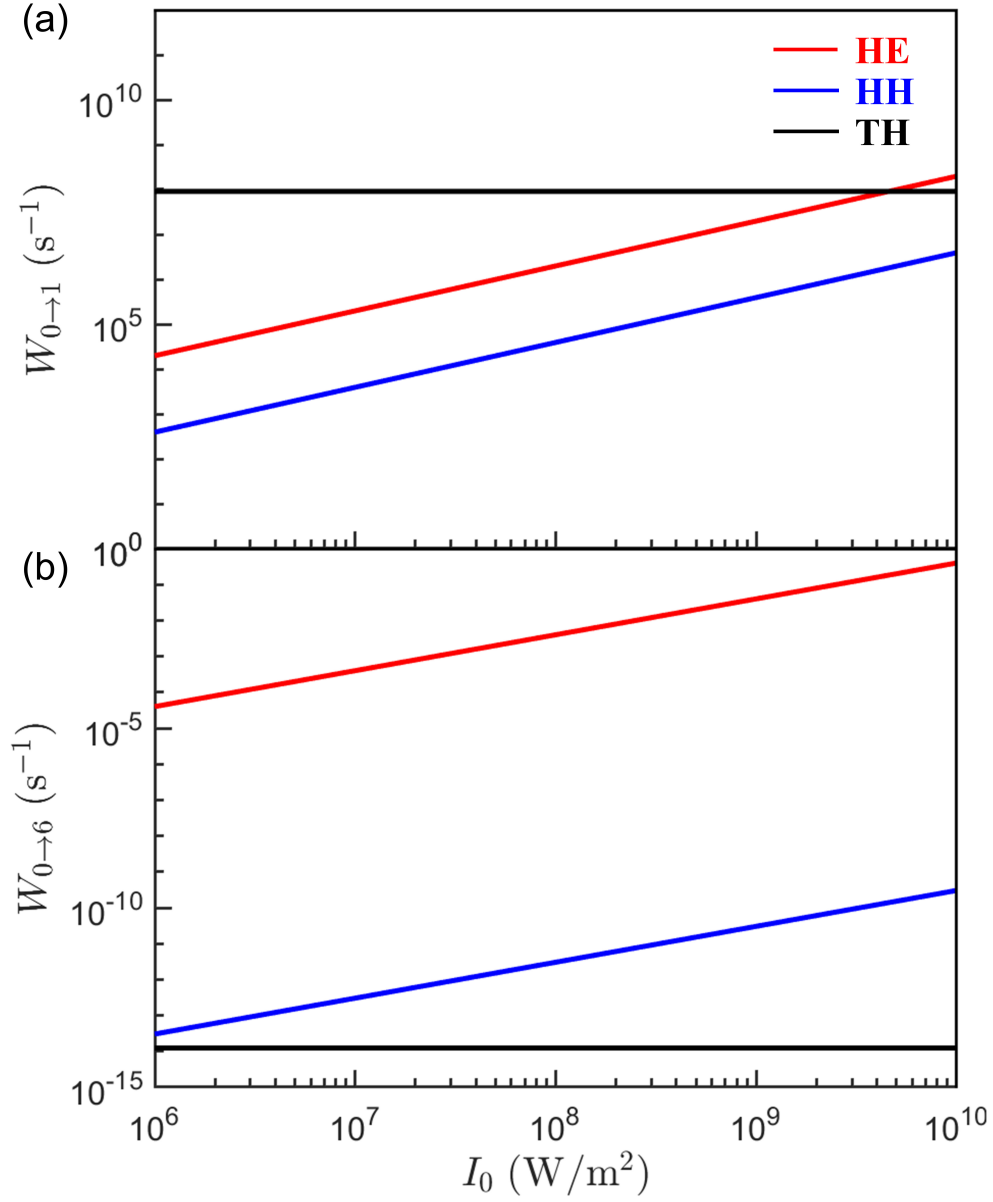


FIG. 5. Light intensity dependence of the vibrational excitation rate with the temperature fixed at 300 K. Contributions from hot electrons (red lines), hot holes (blue lines), and thermal carriers (black lines) to both (a) $n = 0$ to $n = 1$ and (b) $n = 0$ to $n = 6$ excitations are evaluated. Nonthermal carriers remain efficient in activating higher level vibrational excitations, even at low light intensities.

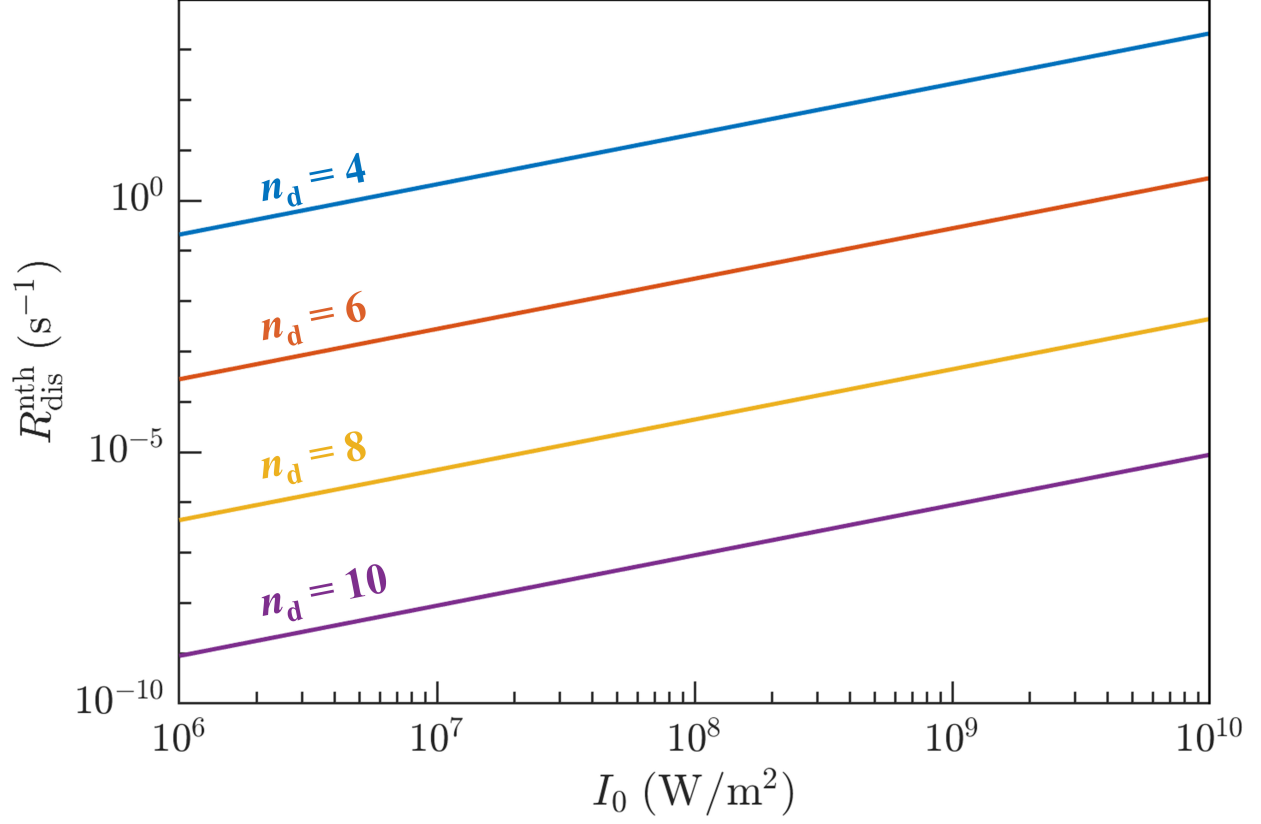


FIG. 6. The nonthermal contribution to the dissociation rate within the DIET mechanism as a function of light intensity at different values of dissociation level. The rate shows linear dependence and possesses larger magnitude at lower dissociation level. Parameters used in the calculations are $h\nu = 3.5$ eV, $T = 300$ K, and $\tau = 100$ fs.

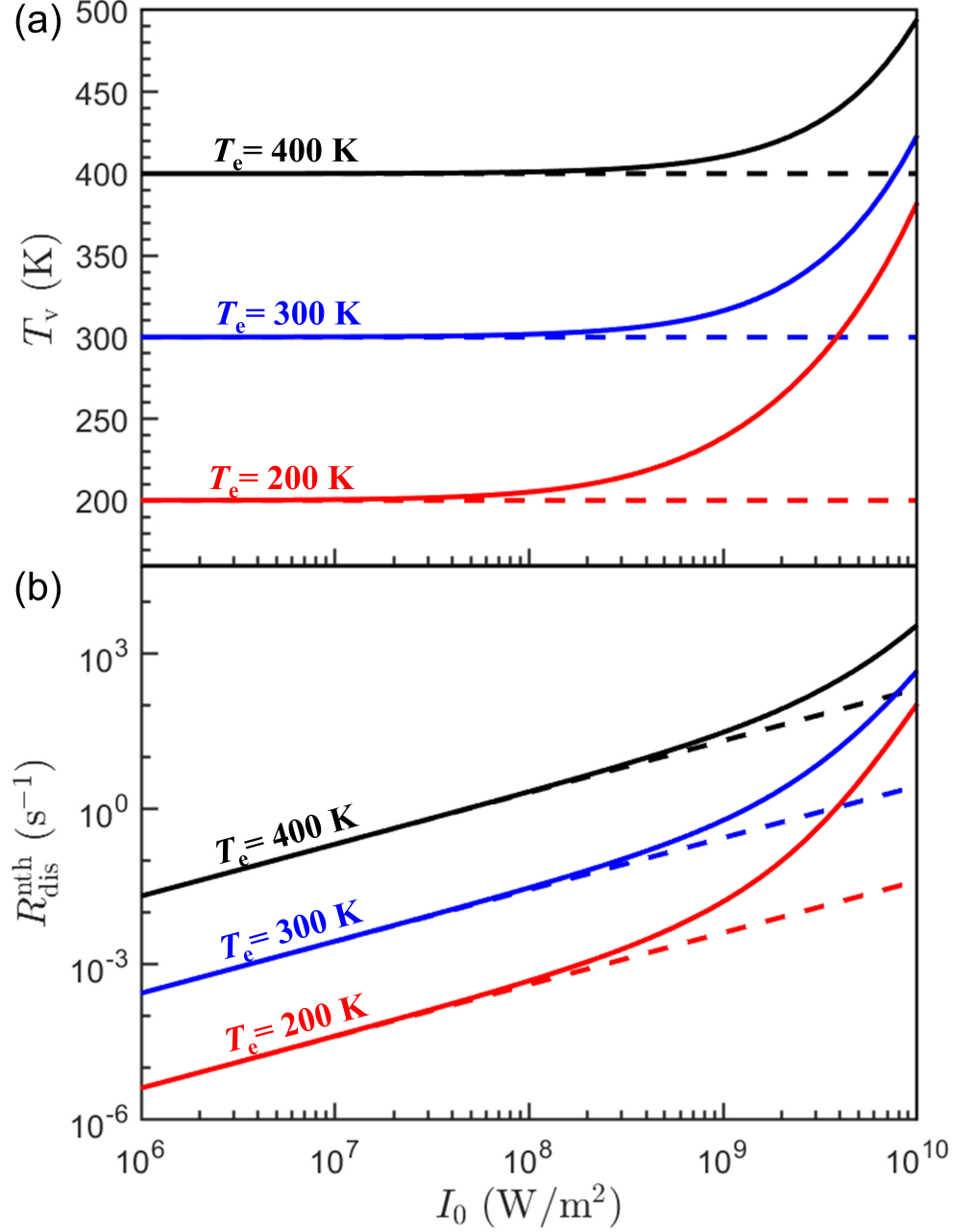


FIG. 7. (a) Light intensity dependence of the vibrational temperature (solid lines) under resonant illumination. As compared to the electronic temperature (dashed lines), dramatic vibrational heating of admolecule can be observed especially at high values of light intensity. (b) The dissociation rates as a function of light intensity in the DIMET regime (solid lines) and are compared to the corresponding DIET curves (dashed lines).

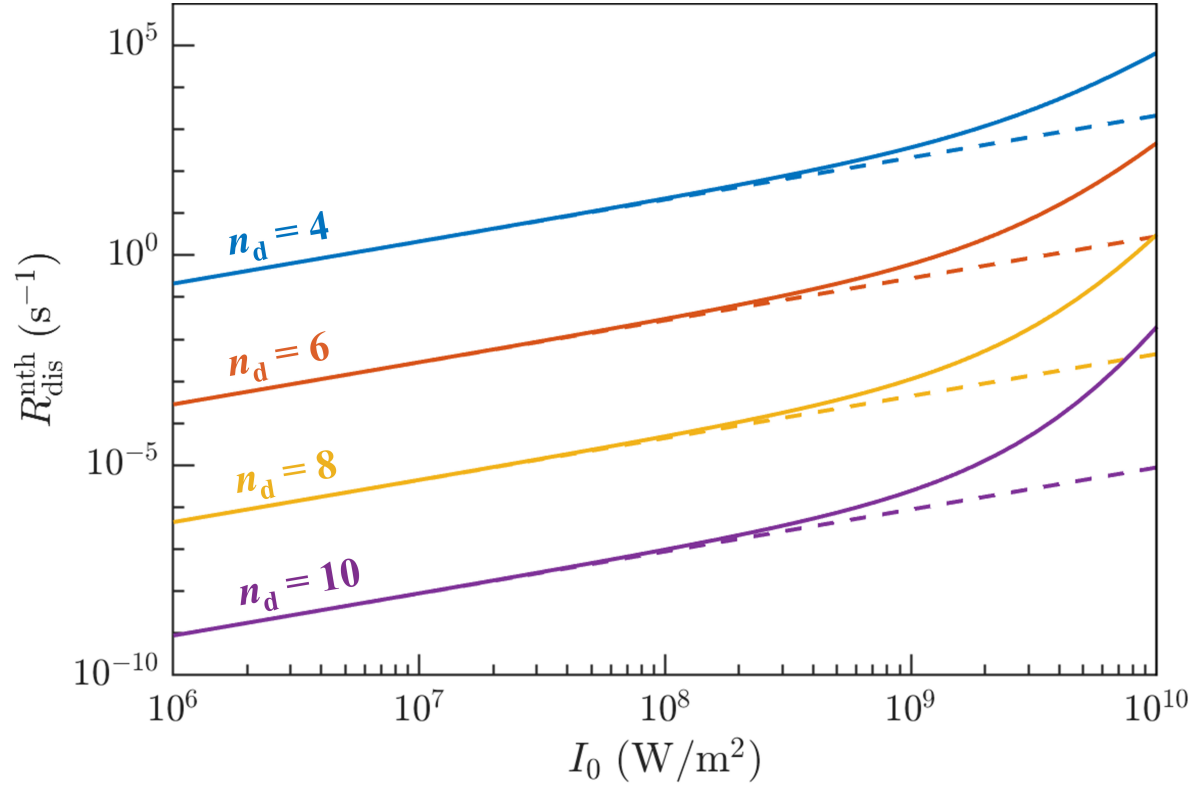


FIG. 8. Light intensity dependence of the nonthermal contribution to the dissociation rate calculated within the DIMET mechanism at different values of dissociation level. The dashed lines are the linear fit of the rates under weak excitation. Clear superlinearity gradually shows up as the light intensity increases.

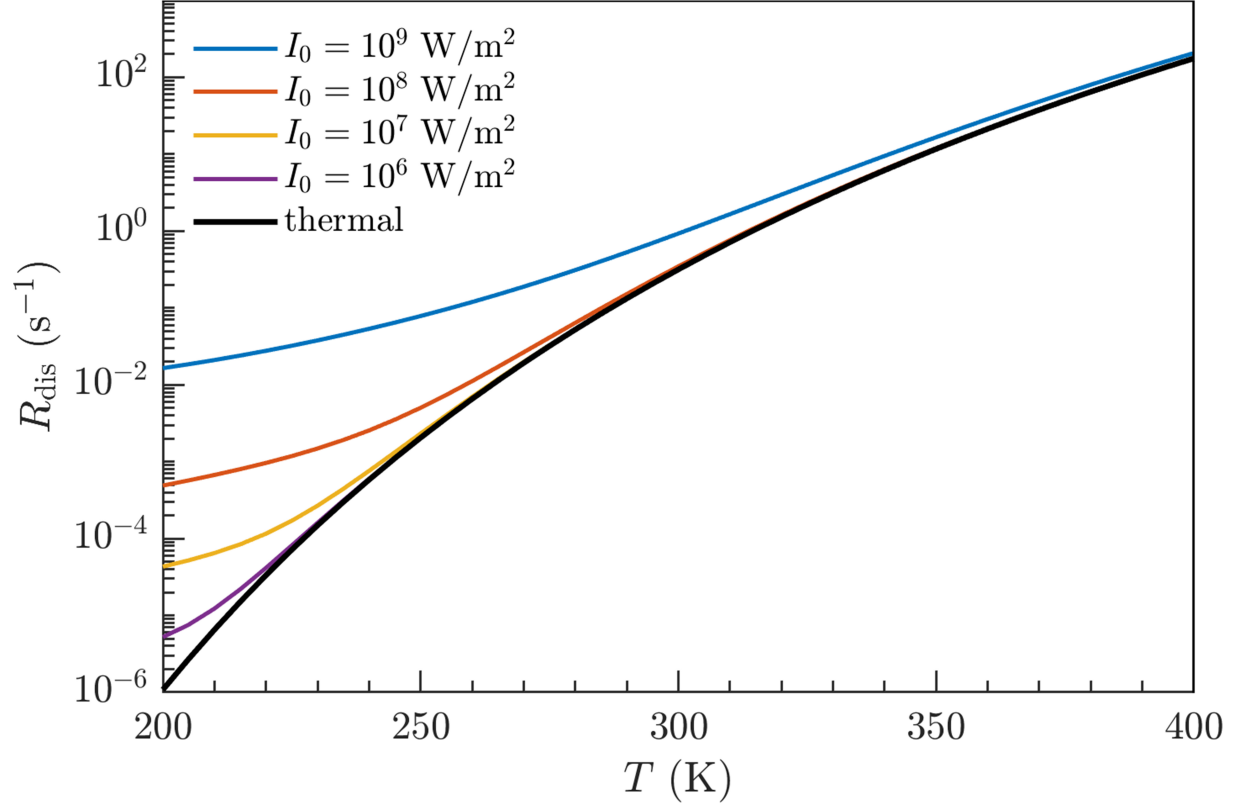


FIG. 9. Temperature dependence of the total dissociation rate at different light intensities under resonant excitation. The nonthermal contributions are dominant in the low temperature regime as compared to the thermal reaction limit (black solid line). All calculations are taken at $n_d = 6$, and $\tau = 100$ fs.